ACS APPLIED MATERIALS & INTERFACES

Research Article

www.acsami.org

Facile Synthesis of Hierarchical Mesoporous Honeycomb-like NiO for Aqueous Asymmetric Supercapacitors

Xiaochuan Ren,[†] Chunli Guo,*[,†] Liqiang Xu,[‡] Taotao Li,[†] Lifeng Hou,[†] and Yinghui Wei*[,†,§]

[†]College of Materials Science and Engineering, Taiyuan University of Technology, Taiyuan, Shanxi 030024, P. R. China

[‡]Key Laboratory of Colloid & Interface Chemistry, Ministry of Education and School of Chemistry and Chemical Engineering, Shandong University, Jinan, Shandong 235000, P. R. China

[§]School of Chemistry and Chemical Engineering, Lvliang College, Lishi Shanxi 033000, China

Supporting Information

ABSTRACT: Three-dimensional (3D) hierarchical nanostructures have been demonstrated as one of the most ideal electrode materials in energy storage systems due to the synergistic combination of the advantages of both nanostructures and microstructures. In this study, the honeycomb-like mesoporous NiO microspheres as promising cathode materials for supercapacitors have been achieved using a hydrothermal reaction, followed by an annealing process. The electrochemical tests demonstrate the highest specific capacitance of 1250 F g^{-1} at 1 A g^{-1}. Even at 5 A g^{-1}, a specific capacitance of 945 F g^{-1} with 88.4% retention after 3500 cycles was obtained. In addition, the 3D porous graphene (reduced graphene oxide, rGO) has been prepared as an anode material for supercapacitors, which displays a good capacitance performance of 302 F g^{-1} at 1 A g^{-1}. An asymmetric supercapacitor has been successfully fabricated based on the honeycomb-like NiO and rGO. The asymmetric supercapacitor achieves a remarkable performance with a specific capacitance of 74.4 F g^{-1}, an energy density of 23.25 Wh kg^{-1}, and a power density of 9.3 kW kg^{-1}, which is able to light up a light-emitting diode.

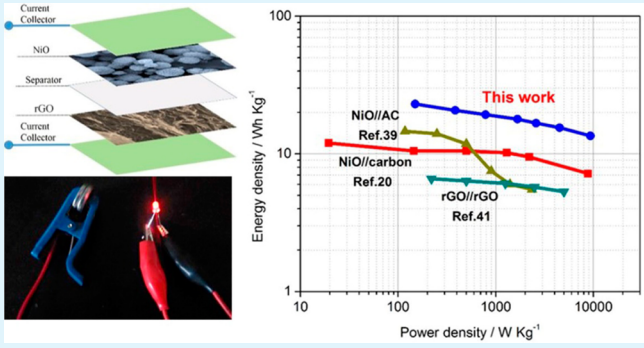

KEYWORDS: *NiO, mesopores, self-assembling, 3D porous graphene, asymmetric supercapacitor*

1. INTRODUCTION

The portable, secure, and low-cost energy storage systems with high capacitance, such as electrochemical supercapacitors and lithium-ion batteries, have attracted attention because of the rapid development of electronic devices. Compared with lithium-ion batteries, electrochemical supercapacitors are one kind of the most promising energy storage devices that can provide a higher power density, faster charge/discharge rate, and longer working lifetime.[1−4] Electrochemical supercapacitors are generally divided into two categories, including electric double-layer capacitors (EDLCs) and pseudocapacitors. The EDLCs store energy by using reversible adsorption of ions at the electrode/electrolyte interface of large-surface-area materials such as porous carbons, carbon nanotubes, and graphenes.[5,6] They always show high power density, long cycle life, and stable cycling performance but share a relatively low specific capacitance.[7] In contrast, pseudocapacitive materials, such as metal hydroxides,[8,9] transition-metal oxides,[10,11] and conducting polymers,[12] can display a remarkably lager pseudocapacitance than the carbon materials through the utilization of multiple oxidation states to realize reversible faradaic reactions. Therefore, we usually assemble asymmetric capacitors by the combination of pseudocapacitive and EDLC materials to achieve high energy density, high power density, and stable cycling life.

NiO pseudocapacitive materials, one of the transition-metal oxides, have attracted great attention because of their higher theoretical specific capacitance (2573 F g^{-1} within 0.5 V) than some other transition-metal oxides (such as MnO_2 and CuO). Furthermore, NiO materials also have a commercial advantage over the binary transition-metal oxides (such as $NiCo_2O_4$, $MnCo_2O_4$, and so on) because of their low cost and ease of preparation. NiO showed a good capacitance performance in the reported literature. However, their performance is greatly dependent on their morphology, surface area, and pore properties.[13,14] For example, the reported coral-like NiO nanobars could exhibit 1085 F g^{-1} at 1 A g^{-1}.[15] Huang et al. reported that the NiO nanosheets deposited on the nickel foams can achieve 674.2 F g^{-1} at 1 A g^{-1}.[16] The mesoporous NiO nanoflake arrays could deliver 400 F g^{-1} at 2 A g^{-1}, as proven by the Tong group.[17] Du et al. reported nano-NiO flower-like microspheres with a maximum specific capacitance

Received: May 12, 2015
Accepted: August 24, 2015
Published: August 24, 2015

DOI: 10.1021/acsami.5b04094
ACS Appl. Mater. Interfaces 2015, 7, 19930−19940

of 762 F g^{-1} at 1 A g^{-1}.[18] The reported specific capacitances of NiO are far away from the theoretical specific capacitance. In addition, the asymmetric supercapacitors based on NiO as the positive electrode material have rarely been studied, and the reported capacitance performance exhibited a small specific capacitance, a low energy density, and a power density. The poor capacitance performance could be due to the limited ion diffusion and fewer electrochemical active sites. The hierarchical mesoporous NiO with a large specific surface area and a large pore volume can be in more contact with the electrolyte and facilitate ion diffusion, which are believed to be more suitable for use as positive electrode materials for the asymmetric supercapacitors.[19,20]

In this study, we controlled the synthesis of hierarchical mesoporous honeycomb-like NiO microspheres and used then to assemble an asymmetric supercapacitor. The honeycomb-like NiO microspheres display a high specific surface area (257 m^2 g^{-1}) and a large total pore volume (1.64 cm^3 g^{-1}), which can achieve a large specific capacitance of 1250 F g^{-1} at a current density of 1 A g^{-1}. Even at 5 A g^{-1}, they also exhibited a high specific capacitance of 945 F g^{-1} with 88.4% retention after 3500 cycles, revealing its superior performance. Some other morphologies of NiO were also prepared for comparison using a similar method by adjusting the pH values. A possible mechanism for the formation of different structures of NiO has been proposed in this paper. Moreover, the three-dimensional (3D) porous graphene with a good capacitance performance has been prepared as an anode material. An asymmetric supercapacitor has been successfully fabricated based on the honeycomb-like NiO and reduced graphene oxide (rGO). The asymmetric supercapacitor achieves a significant performance with a specific capacitance of 74.4 F g^{-1}, an energy density of 23.25 Wh kg^{-1}, a power density of 9.3 kW kg^{-1}, and good cycling stability (88% retention after 2000 cycles), which can successfully light up a low-voltage device such as a light-emitting diode (LED).

2. EXPERIMENTAL SECTION

2.1. Preparation of Honeycomb-like NiO Microspheres. All chemicals were of analytical grade and were used without further purification. In a typical synthesis, 0.3 g of ethylenediaminetetraacetic acid disodium salt (EDTA-2Na), 1.2 g of $NiSO_4{\cdot}6H_2O$, and 0.3 g of urea were dissolved in 15 mL of deionized water. Then the $NiSO_4$ solution was added slowly to the EDTA-2Na solution under constant stirring at room temperature. The color of the mixed solution turned to deep blue. Finally, the urea solution was also poured into the above-mixed deep-blue solution and stirred for 3 min. The pH value of the reaction system was adjusted to 6 by ammonia and a dilute sulfuric acid solution. The obtained solution was transferred to a 60 mL Teflon-lined autoclave, sealed, and kept at 180 °C for 4 h. After that, the reactor was cooled to room temperature. The green powder was collected by filtration and dried at 60 °C. Subsequently, the black product was obtained by annealing the above-mentioned green powders at 300 °C for 2 h with a temperature ramp of 1 °C min^{-1} in an air atmosphere.

2.2. Preparation of the 3D Porous Graphene (rGO). A graphene oxide (GO) solution was initially prepared by a modified Hummers method. The obtained GO solution was first diluted to 2 mg mL^{-1}. Then 40 mL of the diluted GO solution was added to a 60 mL Teflon-lined autoclave and maintained at 180 °C for 20 h. The autoclave was naturally cooled to room temperature. A self-assembled columnar graphene was obtained. Finally, the 3D porous graphene was obtained by vacuum-freeze-drying for 48 h.

2.3. Materials Characterization. Crystallographic information on the as-prepared products was collected using a powder X-ray diffractometer (Bruker D8) equipped with Cu Kα radiation (λ = 0.15418 nm). The morphologies of the samples were recorded by field-emission scanning electron microscopy (SEM; MIRA3 LMH). The high-resolution transmission electron microscopy (HRTEM) images were recorded on a JEOL-2100F transmission electron microscope at 200 kV. The specific surface area was estimated using the Brunauer–Emmett–Teller (BET) method, and the pore-size distribution data were calculated using the Barrett–Joyner–Halenda (BJH) method based on a Quadrasorb Si surface area analyzer (version 5.06). X-ray photoelectron spectroscopy (XPS) spectra were measured on an X-ray photoelectron spectrometer (ESCALAB 250) by referencing the C 1s peak to 284.6 eV. Raman spectra were acquired using a micro-Raman system (LabRAM HR800) with an excitation energy of 2.41 eV (514 nm).

2.4. Electrochemical Measurements. The cyclic voltammetry (CV), galvanostatic charge and discharge (GCD), and electrochemical impedance spectroscopy measurements were carried out on a CHI 760E electrochemical workstation in a 6 M KOH aqueous solution with Hg/HgO as the reference electrode, a platinum foil (1 × 2 cm^2) as the counter electrode, and the annealed samples as the working electrode. The working electrodes were prepared by mixing the as-prepared materials, acetylene black, and poly(vinylidene difluoride) in a mass ratio of 8:1:1 in 1-methyl-2-pyrrolidinone. The mixture was ground adequately to form a slurry and then coated on one side of the pretreated nickel foam with 12 mm diameter at a pressure of 10 MPa. Finally, they were dried in a vacuum oven at 60 °C for 10 h. The mass of the active material coated on each electrode was about 3 mg. All of the experiments were done at room temperature.

The specific capacitance C_s (F g^{-1}) value of the supercapacitor electrode materials can be calculated from CV by using the following equation:

$$C_s = \frac{1}{vw(V_a - V_c)} \int_{V_a}^{V_c} I \, dV \tag{1}$$

Here v (V s^{-1}) is the sweep rate, w (g) is the mass of active material, I (A) is the cathodic or anodic current, and V_a to V_c (V) is the potential window.

The specific capacitances were also calculated from the charge/discharge curves according to the following equation:

$$C_s = \frac{I\Delta t}{m\Delta V} \tag{2}$$

where I (A g^{-1}) is the discharging current, m (g) is the mass of the electrode materials, Δt (s) is the discharge time, and ΔV (V) is the discharge potential window.

2.5. Preparation of the Asymmetric Supercapacitor. The asymmetric supercapacitor was fabricated based on the honeycomb-like NiO microspheres as the positive electrode and rGO as the negative electrode with a polypropylene separator. A 6 M KOH solution was used as the electrolyte. The asymmetric supercapacitor was encapsulated to prevent leakage of the electrolyte. The specific capacitance and energy and power densities of the asymmetric supercapacitor device were all calculated based on the total mass of both the positive and negative electrodes excluding the current collector.

The energy density (Wh kg^{-1}) of the asymmetric supercapacitor device was calculated from the discharge curves from the equation

$$E = \frac{C_s \Delta V^2}{2} \tag{3}$$

where C_s (F g^{-1}) is the specific capacitance of the asymmetric supercapacitor device and ΔV (V) is the potential range, and the power density (W kg^{-1}) was determined using the following equation:

$$P = \frac{E}{\Delta t} \tag{4}$$

where E (Wh kg^{-1}) is the energy density and Δt (h) is the discharge time.

DOI: 10.1021/acsami.5b04094
ACS Appl. Mater. Interfaces 2015, 7, 19930–19940

3. RESULTS AND DISCUSSION

3.1. Detailed Analysis of NiO Prepared as the Cathode Material.

Morphologies and Structures. SEM and TEM were used to investigate the structure and morphology of the as-synthesized materials. Parts a and b of Figure 1 show the

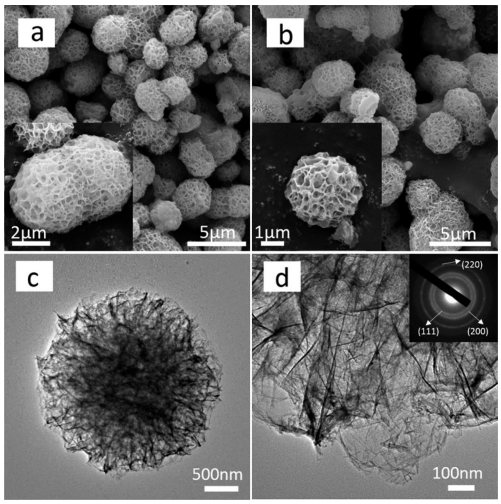

Figure 1. (a) SEM image of the $Ni(OH)_2$ precursor and (b) the obtained honeycomb-like NiO after an annealing treatment of $Ni(OH)_2$. The insets of parts a and b are their corresponding high-resolution SEM images. Typical TEM (c) and HRTEM (d) images of honeycomb-like NiO. The inset of part d is the SAED image.

morphologies of the honeycomb-like $Ni(OH)_2$ and NiO, respectively. Their morphologies are hierarchical microspheres, and their average sizes are about 3−5 μm. From the high-resolution SEM images, it can be seen that the honeycomb-like microspheres consisted of random self-assembled nanosheets. After annealing treatment, the morphology of NiO were well-maintained with an unchanged size because of the low calcination temperature and slow heating rate. Figure 1c shows the TEM image of NiO, and it further proves that two-dimensional thin nanosheets were interwoven together to form a hierarchical superstructure. Figure 1d is the HRTEM image. The selected-area electron diffraction (SAED) pattern in the inset of Figure 1d produces a pattern of concentric rings, indicating its polycrystalline structure.

Furthermore, in order to demonstrate the effect of the pH value on the structure and morphology during the hydrothermal route and the influence of their morphology on the capacitance performance, we also adjusted the pH value by ammonia and a dilute sulfuric acid solution to 2, 8, and 11. In order to identify them, we named the products prepared at the pH values of 2, 6, 8, and 11 from the hydrothermal route as N1, N2, N3, and N4, respectively, and their corresponding annealing products are C1, C2, C3, and C4, respectively. Accordingly, we must emphasize that the honeycomb-like α-$Ni(OH)_2$ precursor is named as N2 and the NiO product after annealing treatment as C2.

The morphological characteristics of the $Ni(OH)_2$ products (N1, N3, and N4) and NiO (C1, C3, and C4) are also shown in Figure S1. The morphology of sample N1 is cocoon-like, the filiform structure of which can be seen on the surface of the microspheres. The morphology of sample N4 is flower-like, and it consists of self-assembled micropetals. Sample N3 shows varied shapes and size characteristics, and it can be divided into two types of morphologies according to the surface appearance: a honeycomb-like oversize ball similar to that of sample N2 and a flower-like morphology similar to that of sample N4. Hence, the morphologies of the $Ni(OH)_2$ products transformed from small-size cocoon-like structures to large-size microflowers with increasing pH values. As shown in Figure S1, the morphologies of NiO can sustain the original shapes of their corresponding $Ni(OH)_2$ precursors after the annealing treatment without obvious deformation.

The purity and phase structure of the powders are examined by X-ray diffraction (XRD). Figure 2 shows the XRD patterns

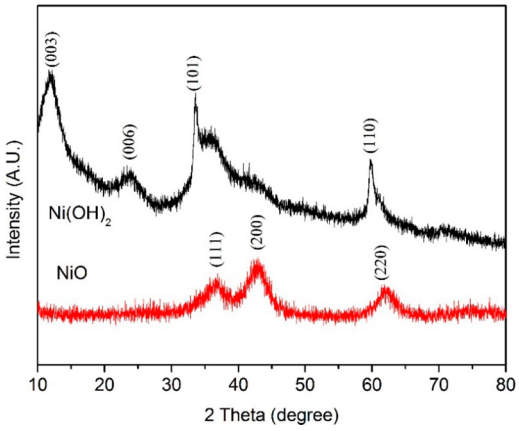

Figure 2. XRD patterns of the honeycomb-like NiO and α-$Ni(OH)_2$ precursor.

of the α-$Ni(OH)_2$ precursor synthesized by the hydrothermal route and the honeycomb-like NiO after heating in an air atmosphere. The peaks from the black curve at about 11.3°, 22.8°, 33.5°, and 59.9° are indexed as (003), (006), (101), and (110) reflections of rhombohedral α-$Ni(OH)_2$ (JCPDS 38-0715), similar to the reported literature.[21] The diffraction peaks from the red curve detected at 37.1°, 43.1°, and 62.6° for the (111), (200), and (220) planes of face-centered-cubic NiO (JCPDS 89-7130). The broad and middle-intensity peaks indicate that the sizes of α-$Ni(OH)_2$ and NiO are small and that they have nanocrystalline nature.

The XRD patterns of the products synthesized at different pH values are also shown in Figure S2. As shown in Figure S2a, the diffraction peak intensities of sample N1 are low and weak, suggesting poor crystallinity, which can also match with α-$Ni(OH)_2$. The sharp and high-intensity diffraction peaks of sample N4 are ascribed to hexagonal β-$Ni(OH)_2$ (JCPDS 14-0117). No evidence of other impurities were observed by XRD, suggesting that the well-crystallinity and purity of β-$Ni(OH)_2$ were ensured in our hydrothermal route at pH 11. Figure S2a also shows that sample N3 is composed of α-$Ni(OH)_2$ and β-$Ni(OH)_2$. On the basis of the XRD results, we can conclude that α-$Ni(OH)_2$ can convert to β-$Ni(OH)_2$ with increasing pH values. That is, the α-$Ni(OH)_2$ phase easily forms in acidic or weak basic systems, and the β-$Ni(OH)_2$ phase tends to be stable under strong alkaline conditions. Figure S2b shows typical XRD patterns of samples after heating. All of the broad diffraction peaks of the four samples match those of the face-centered-cubic NiO. The average size of samples C1−C4 can be calculated by Debye−Scherrer's formula from the half-width of peaks (111), (200), and (222) as 3.3, 3.2, 4.0, and 5.1 nm, respectively.

DOI: 10.1021/acsami.5b04094
ACS Appl. Mater. Interfaces 2015, 7, 19930−19940

XPS analysis of the honeycomb-like NiO (Figure S3) is given to exhibit the binding energy. In the Ni 2p spectra (Figure S3a), the peak appearing at 855.2 eV has a satellite peak (861.1 eV) related to the Ni $2p_{3/2}$ levels and the peak located at 873.1 eV has a satellite peak (878.8 eV) belonging to the Ni $2p_{1/2}$ levels. The binding energies of the Ni 2p core levels are consistent with those in the previous report on NiO.[22,23] The O 1s spectrum (Figure S3b) consists of two peaks after deconvolution according to the previous reports. The fitting peak exhibited at 529.5 eV is a metal−oxygen bond of Ni−O in NiO. The peak at 531.2 eV demonstrates the presence of nickel hydroxides and oxyhydroxides, including defective nickel oxide with absorbed hydroxyl groups.[24]

An illustration of the morphological evolution of samples N1−N4 is shown in Scheme 1. The possible formation process of samples N1−N4 can be included by the mechanisms of self-aggregation and oriented growth, which are reported by other researchers.[25,26] In our works, the pH has an important influence on the nucleation process. The highly concentrated OH^- in a high-pH system can act a sufficient source for the formation of $Ni(OH)_2$ nuclei and also promote the rapid growth of the $Ni(OH)_2$ nuclei. Because of the existence of abundant NH_3, the nuclei will tend to form large petals of $Ni(OH)_2$.[11] In a low-pH system, however, OH^- and NH_3 derive from the slow decomposition of urea in high temperature and their relatively low concentration can slow down the formation and growth of $Ni(OH)_2$ nuclei, and the existence of a certain amount of $EDTA^{2-}$ may be favorable for the formation of small flakes of $Ni(OH)_2$ because of the strong complexation property of $EDTA^{2-}$. It is worth mentioning that the relatively high concentration ratio of $EDTA^{2-}$ compared to NH_3 in a lower pH system may tend to form the filiform structure of $Ni(OH)_2$ shown as sample N1. During the subsequent growth stages, the $Ni(OH)_2$ slices will tend to self-aggregate to decrease their surface energy by reducing exposed areas. Also, the Ostwald ripening process will lead to the formation of larger-size $Ni(OH)_2$ microspheres with various morphologies according to the different systems.[27]

Scheme 1. Illustration of the Morphological Evolution of Samples N1−N4

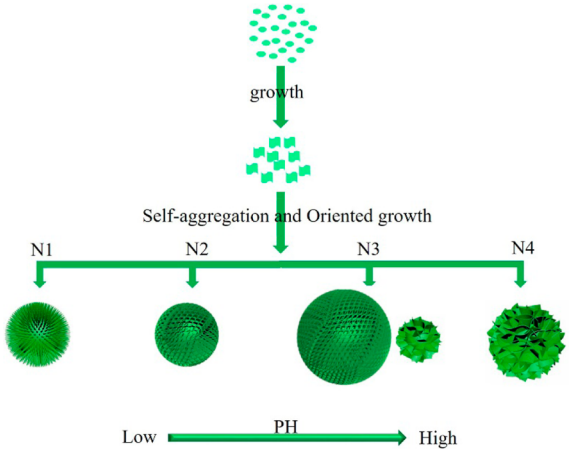

Surface Area and Porosity Analysis. The nitrogen adsorption−desorption isotherms and the BJH pore-size distribution of samples C1−C4 are shown in Figure 3. It can be seen that all four annealed samples exhibit an irreversible type IV isotherm in the Brunauer classification, which is the typical feature of a mesoporous structure.[28] According to the IUPAC classification, the characteristic hysteresis loops observed in the range of 0.5−1.0 P/P_0 in the four samples are ascribed to type H3 loops, indicating the presence of slit-shaped pores. The specific BET surface areas of samples C1−C4 (Table 1, obtained or calculated from the BET reports) are

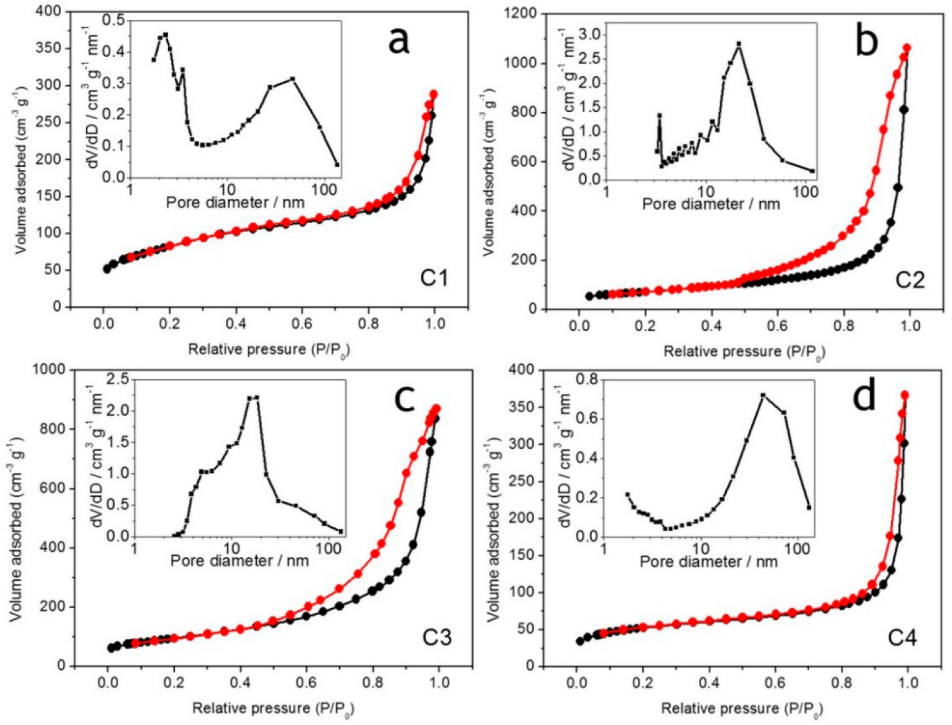

Figure 3. Nitrogen adsorption−desorption isotherm of samples C1 (a), C2 (b), C3 (c), and C4 (d). The insets in parts a−d are the BHJ pore-size distribution plots.

DOI: 10.1021/acsami.5b04094
ACS Appl. Mater. Interfaces 2015, 7, 19930−19940

Table 1. Quantitative Structural Parameters for Different NiO Samples

sample	surface area (m^2 g^{-1})	average pore size (nm)	total pore volume (cm^3 g^{-1})	micropore area (m^2 g^{-1})
C1	298	5.9	0.446	17
C2	257	25	1.64	6
C3	339	15.8	1.34	23
C4	191	11.8	0.567	58

298, 257, 339, and 191 m^2 g^{-1}, and their average pore sizes are 5.9, 25, 15.8, and 11.8 nm, respectively. It is reported that the large surface area could improve the capacitive performance by facilitating electrolyte diffusion into the active sites of the redox reaction, while the surface area is not the unique influencing parameter for the capacitance but an increasing tendency of the specific capacitance.[29,30] From parts a−d of Figure 3, the small slopes of the adsorption branches in the BET isotherms indicate the presence of a small percentage of micropores from 0 to 0.04 P/P_0, consistent with the micropore surface area data in Table 1.[31] The micropore surface areas of samples C1−C4 are 17, 6, 23, and 58 m^2 g^{-1}, and their corresponding proportions share 5.7%, 2.3%, 6.8%, and 30.4% of the total surface areas. Samples C2 and C4 are the smallest and largest proportions of the micropore areas. Generally, high proportions of mesopore areas can contribute to achieving a high-energy and high-power storage. Hence, the difference between the proportions of micropore and mesopore areas has an important influence on the EDLC and pseudocapacitance.[32,33] The insets in parts a−d of Figure 3 are the BHJ pore-size distribution plots. Samples C1 and C2 present a multimodal-type pore-size distribution with maxima peaks centered at 2.3 and 50 nm and at 3.3 and 20 nm, respectively. Samples C3 and C4 show a unimodal-type pore-size distribution with maxima peaks centered at 18 and 50 nm, respectively. Moreover, compared with the ordinate scales of the pore-size distribution curves in the insets of Figure 3, the ordinate scale in the curve of sample C2 displays the highest value. Overall, the honeycomb-like NiO demonstrates the presence of a larger fraction of mesopores. In addition, it also shows the largest total pore volume (1.64 cm^3 g^{-1}). Commonly, the large amount of mesopores, high specific surface area, and large total pore volume of the porous materials can achieve better electrochemical performance because they provide low-resistant pathways and a short distance for ion diffusion during the electrochemical tests. Therefore, the electrochemical performance of honeycomb-like NiO may be better.

Electrochemical Properties. CV is generally used to characterize the capacitive behavior of NiO powder. Figure 4 shows the typical CV curves of samples C1−C4 at different scan rates for the fifth scan cycle in a 6 M KOH aqueous solution. A set of broad redox peaks corresponding to Ni^{2+}/Ni^{3+} are clearly found in the curves of four samples, suggesting their typical faradaic capacitance features. The reversible reaction between Ni^{2+} and Ni^{3+} took place on the surface of the NiO electrode and can be expressed as the following reaction:[34]

$$NiO + OH^- \Leftrightarrow NiOOH + e^- \quad (5)$$

The asymmetrical redox peaks can be observed in all of the NiO configurations from Figure 4. This common phenomenon for the pseudocapacitor can lead to irreversibility of the redox process, which can be attributed to the generation of polarization and ohmic resistance by faradaic redox reactions

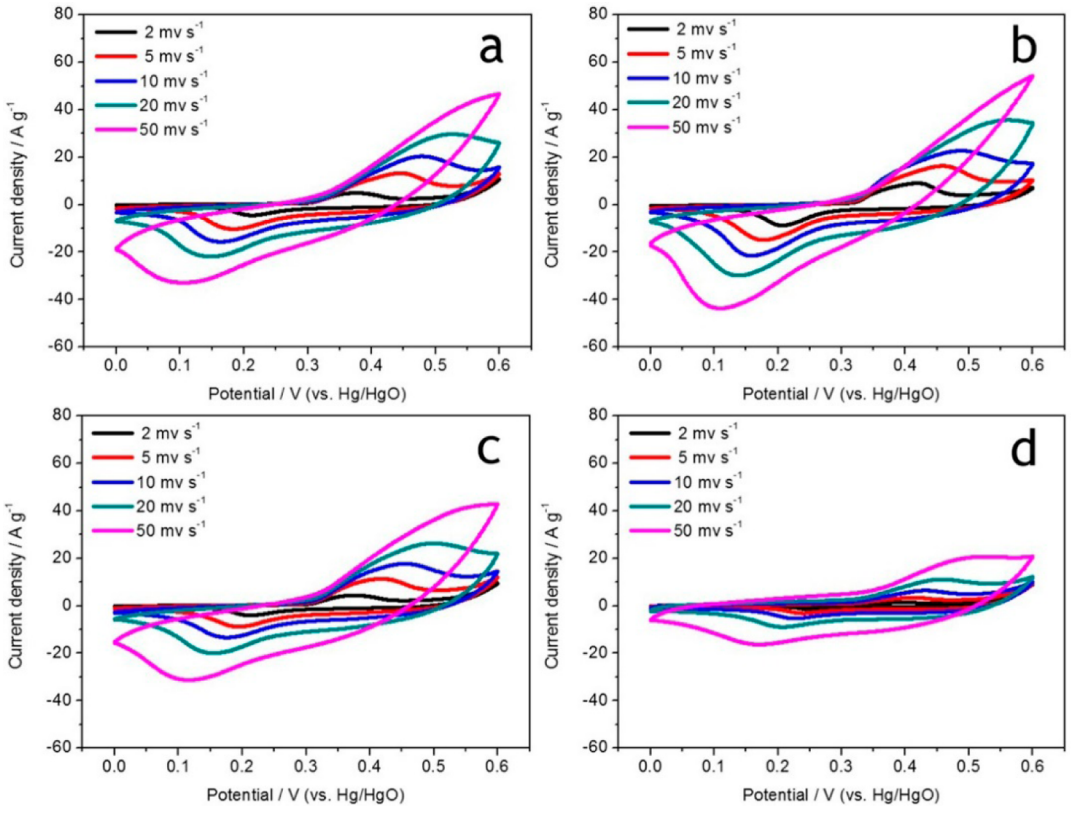

Figure 4. CV curves of samples C1 (a), C2 (b), C3 (c), and C4 (d) for the fifth scan cycle at various rates of 2, 5, 10, 20, and 50 mV s^{-1}.

DOI: 10.1021/acsami.5b04094
ACS Appl. Mater. Interfaces 2015, 7, 19930−19940

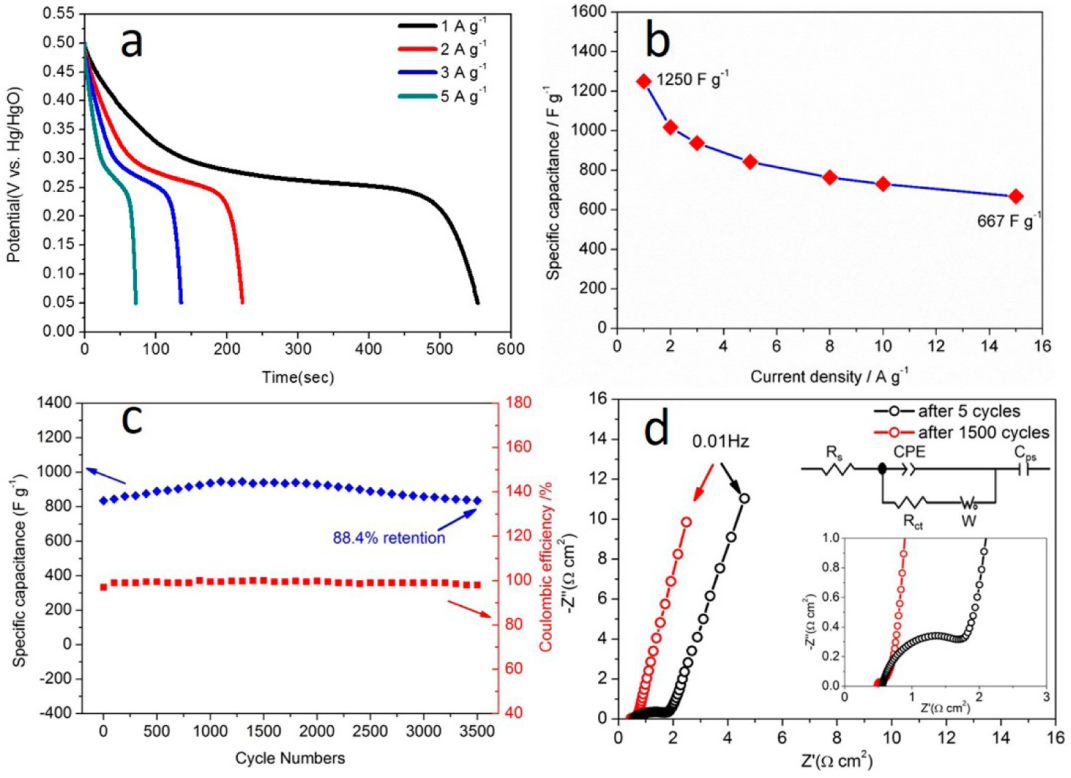

Figure 5. (a) Discharge curves for the honeycomb-like NiO electrodes (sample C2) measured at different current densities. (b) Variation in the specific capacitance of the honeycomb-like NiO electrode as a function of the current density. (c) Cycling performance and columbic efficiency at a current density of 5 A g^{-1}. (d) Nyquist plots of the honeycomb-like NiO electrode after 5 and 1500 cycles. The inset shows an equivalent circuit and an enlarged view of the Nyquist plots for the electrode.

and ion diffusion within the porous electrode during the redox reaction process.[35] Furthermore, the slight negative/positive shifts in the redox peaks are observed with increasing potential scan rates mainly due to the increasing internal diffusion resistance of the pseudocapacitive materials.[36]

Table S1 lists the specific capacitances for samples C1−C4 at scan rates of 2−50 mV s^{-1}. Their specific capacitances all decreased gradually with increasing scan rates. At a lower scan rate of 2 mV s^{-1}, the electrolyte ions had sufficient time to diffuse into the inner surface of the electrode materials, resulting in a high electrochemical utilization of electroactive materials, while at a higher scan rate of 50 mV s^{-1}, the redox reaction took place only at the outer surface and resulted in a capacitance decrease. Sample C2 shows the highest specific capacitance at different scan rates thanks to its special structure with a larger electroactive surface area, a lower proportion of micropore area, and a larger pore volume. The smaller pore volume of sample C1 could be bad for permeation of the electrolyte and lead to a worse charge storage performance. A larger proportion of micropores of samples C3 and C4 could restrain ion diffusion of the electrolyte and diminish the active sites for the redox reaction, resulting in their worse capacitive properties.

Figure 5a exhibits the discharge curves of the honeycomb-like NiO at different current densities from 1 to 5 A g^{-1}. The nonlinear discharge curves confirm the pseudocapacitive properties of the NiO electrodes, in agreement with the CV tests.[27] The specific capacitance of NiO is up to 1250 F g^{-1} at 1 A g^{-1} (Figure 5b). Even at 15 A g^{-1}, the specific capacitance is still as high as 677 F g^{-1}. The honeycomb-like NiO offers a higher specific capacitance than many other reports in the past few years, such as a specific capacitance of 567 F g^{-1} at 1 A g^{-1} reported by Purushothaman et al.,[37] 675 F g^{-1} at 2 A g^{-1} for NiO nanotube arrays reported by Cao et al.,[38] and 1060 F g^{-1} at 1 A g^{-1} for NiO ultrathin nanosheets reported by Yao et al.[39] Although the honeycomblike NiO has a low electrical conductivity (the calculated value is 3.344 × 10^{-6} S m^{-1} and the related details can be obtained from the Supporting Information), charge storage is mainly achieved through the surface redox reactions for the pseudocapacitance materials. The enhanced specific capacitance of the honeycomb-like NiO was related to its special morphology and rich mesoporosity characteristic for a large pore volume (1.64 m^3 g^{-1}). This special structure can easily absorb the electrolyte and produce an area acting as an "ion-buffering reservoir" to accommodate OH^- ions for the redox reaction. In this way, the contacts between the electrolyte and electrode materials are increasing and the subsequent diffusion lengths for the electrolyte ions are shortened. Hence, the ion diffusion in the charge/discharge process is accelerated.[40,41] The discharge curves and specific capacitances of samples C1, C3, and C4 at different current densities are also shown in Figure S4. From the curves shown in Figure S4d, sample C2 exhibits the highest specific capacitance at different current densities compared with the other samples. The capacity retention of sample C3 with a large pore volume of 1.34 m^2 g^{-1} is also high with an increase of the current densities. Yet, it is poor for sample C1 because of its low pore volume (0.446 m^3 g^{-1}), although it shows a larger specific surface area than sample C3. The small specific surface area, low pore volume, and large proportion of micropore areas of sample C4 codetermine its very low specific capacitance.

DOI: 10.1021/acsami.5b04094
ACS Appl. Mater. Interfaces 2015, 7, 19930−19940

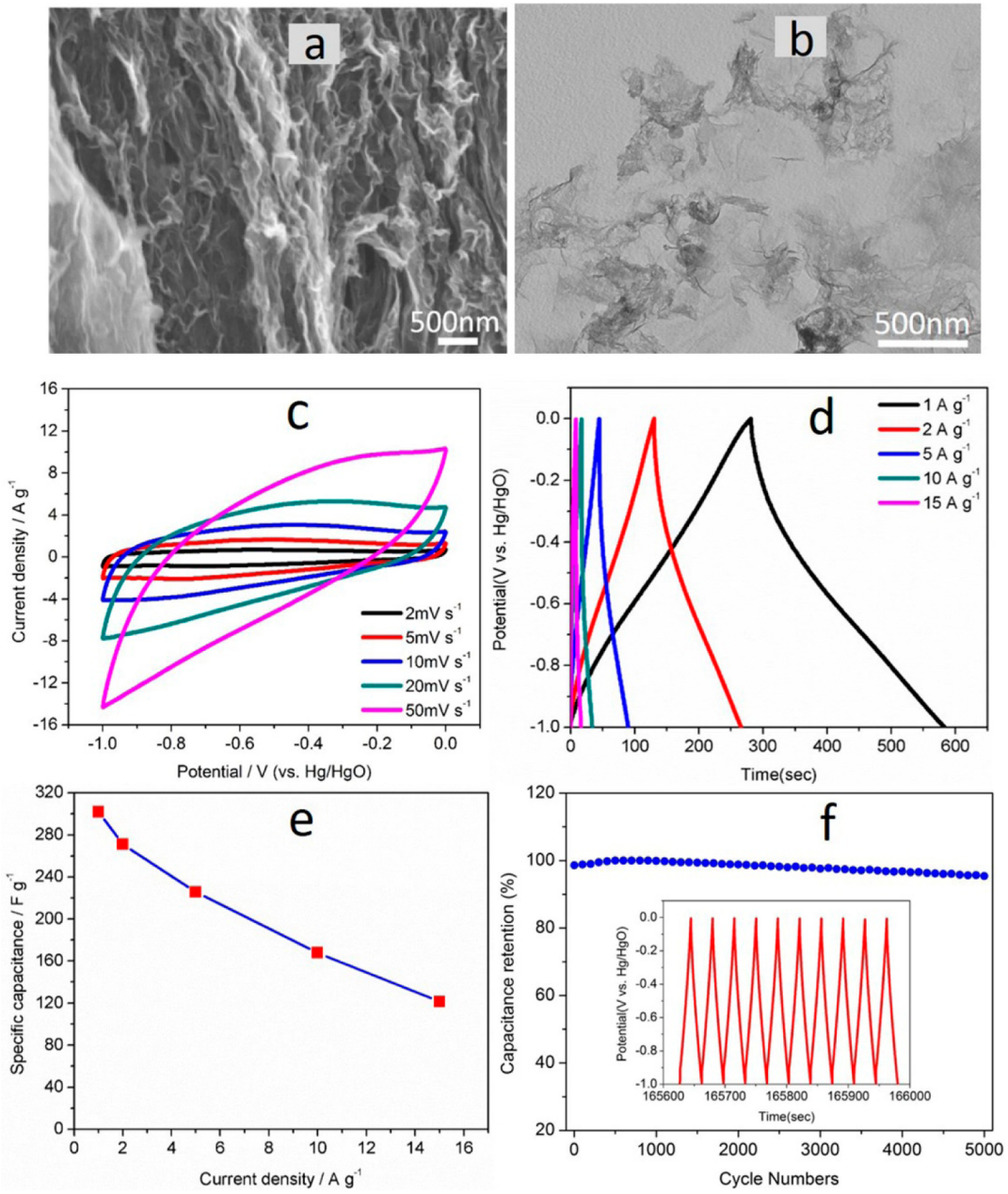

Figure 6. SEM (a) and TEM (b) images of rGO. (c) CV curves of rGO at different scan rates. GCD curves (d) and specific capacitances (e) of rGO at different current densities. (f) Cycling performance of rGO at a current density of 10 A g^{-1}. The inset shows the charge/discharge curves of the last 10 cycles of the rGO electrode.

Figure 5c displays the cycling performance and columbic efficiency of the honeycomb-like NiO at a current density of 5 A g^{-1} for 3500 cycles. The specific capacitance increases slowly from 832 to 945 F g^{-1} before 1100 cycles, then remains steady at 2000 cycles, and soon slowly drops to 835 F g^{-1} by 3500 cycles. Its degradation rate is about 11.6%. The special capacitance of sample C2 has a significant increase of 12% at 2000 cycles. This phenomenon is explained by its porous superstructures. The electrolyte takes more time to penetrate into the microscale honeycomb-like structure, which causes more sites to activate as the test proceeds.[42] In addition, some loose flakes broken from NiO superstructures after the first few cycles would attach to the nearby rigid flakes rather than fall off from the entirety, which would produce larger surface area and more active sites than those of the original structures. Meanwhile, it will partly increase the number of diffusion channels for ions in the electrolyte. The columbic efficiencies of sample C2 are also shown in Figure 5c. It remains as high as 98% over the extended charge/discharge cycles, indicating better cycling performance. Figure 5d displays the Nyquist plots of the honeycomb-like NiO after 5 and 1500 cycles. Also, the inset shows the high-frequency region of the impedance plot and equivalent circuit diagram. In the fitting circuit, R_s is the solution resistance and R_{ct} is the charge-transfer resistance. CPE and C_{ps} are the constant phase element and faradaic pseudocapacitance, respectively.[18] The solution resistance is composed of ionic and electronic resistances, the inherent resistance of the electrode materials, and the contact resistance between the electrode and current collector interface. The charge-transfer resistance is the surface property of the porous

DOI: 10.1021/acsami.5b04094
ACS Appl. Mater. Interfaces 2015, 7, 19930−19940

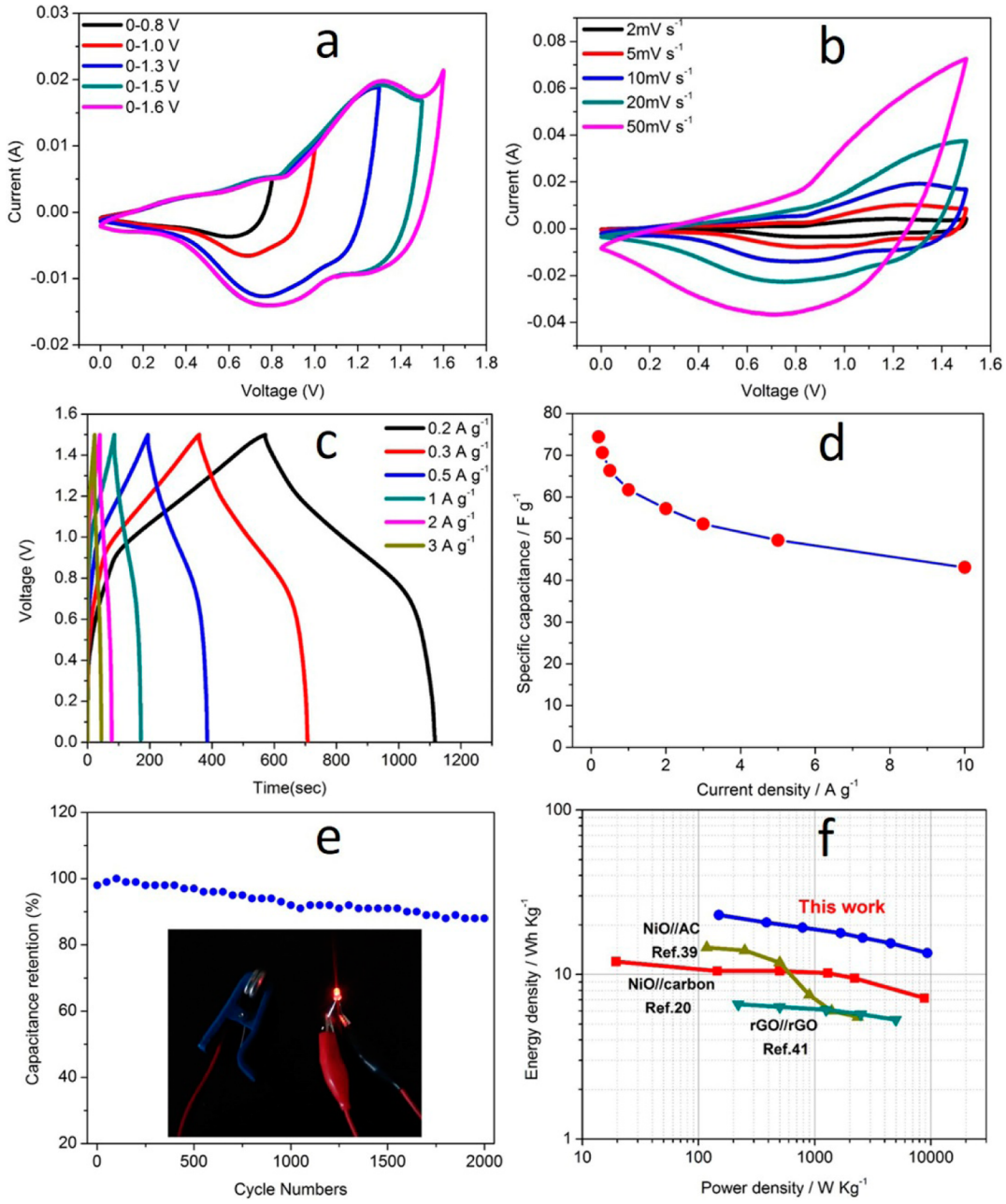

Figure 7. CV curves of the NiO//rGO asymmetric supercapacitor device at different voltage windows (a) and different scan rates (b). GCD curves (c) and specific capacitances (d) of the NiO//rGO device at different current densities. (e) Cycling performance of the NiO//rGO device at a current density of 2 A g^{-1}. The inset is a digital photograph of the lighted LED by the double asymmetric supercapacitor cell. (f) Ragone plot of the NiO//rGO device. The values reported previously for other NiO-based devices are given here for a comparison.

electrode and is related to the electrolyte accessible area of the electrode. R_s and R_{ct} are 0.48 and 0.14 Ω, respectively, after 1500 cycles but are smaller after 5 cycles (0.54 and 1.27 Ω, respectively). This can be attributed to the activation of the active material with the production of more active sites to promote OH^- ion contact with the electrode surface as the test proceeds. Moreover, the results also show the good stability of the as-prepared NiO materials and fit well with the results of the cycling performance. The slopes of the impedance plots at the lower frequency range correspond to a W, which describes the diffusive resistance of the electrolytic ion in the NiO electrode pores. After 1500 cycles, the slope at the lower frequency range is nearly unchanged, confirming the good stability and good capacitor behavior of the NiO material. The Nyquist plots after 5 cycles of samples C1−C4 as well as the equivalent circuit diagram are also presented in Figure S6 for comparison. The charge-transfer resistance follows the order C2 < C1 < C3 < C4, confirming that the honeycomb-like NiO exhibits a larger electroactive surface area than the others. In addition, the higher value of the slope in plots for C2 compared to the other samples indicates faster electrolytic ion diffusion within the NiO structure.[43]

3.2. Brief Analysis of Graphene Prepared as the Anode Material. The SEM image in Figure 6a reveals that rGO has an interconnected 3D porous network with pore sizes ranging from submicrometers to micrometers. The porous feature can be clearly seen from the high-resolution SEM images in Figure S7b. Moreover, as shown in the TEM (Figure

DOI: 10.1021/acsami.5b04094
ACS Appl. Mater. Interfaces 2015, 7, 19930−19940

6b) and SEM (Figure S7a) images, rGO is composed of ultrathin graphene nanosheets. The phase structures of rGO and GO were examined by XRD (Figure S8a). The curve of GO displays a peak at $2\theta = 11.6°$, which corresponds to an interlayer distance of 0.76 nm because of the presence of some functional groups between the layers such as carboxyl, hydroxyl, and epoxy. The curve of rGO shows a broad peak at $2\theta = 24.2°$, indicating its poor ordering characteristic. The structural changes from GO to rGO were investigated by XPS. The C 1s XPS spectra of GO and rGO (Figure S8b,c) were fitted into four individual peaks that correspond to carbon atoms in different functional groups: nonoxygenated C−C bonds at 284.6 eV, C−O at 286.1 eV, C═O at 287.8 eV, and O−C═O at 288.9 eV.[44] After hydrothermal reduction, the oxygen species of C−O, C═O, and O−C═O of rGO are much smaller than those of GO, as shown in Figure S8c, indicating that most of the oxygen-containing functional groups in GO were removed. The changes of the structure are further studied by Raman spectroscopy (Figure S8d). As shown in the figure, the peak for rGO (1584 cm^{-1}) at the G band is down-shifted compared with that of GO (1598 cm^{-1}), indicating that the hexagonal network of carbon atoms in rGO recovers with defects from the structure of rich isolated double bonds in GO.[45] The I_D/I_G ratio of GO is 0.9 and increases to 1.12 in rGO, which indicates that some defects are introduced in rGO because of hydrothermal reduction. The defects related to the disordered carbon structure such as the vacancy, boundaries, and amorphous structure can provide more active sites for charge storage and enhanced electrochemical properties.

The CV curves of rGO show similar rectangular shape at different scan rates with a potential window of −1.0 to 0.0 V (vs Hg/HgO) in a 6 M KOH electrolyte solution (Figure 6c), which indicates the typical double-layer capacitance. The GCD curves of rGO are relatively symmetrical and linear, which also indicates double-layer capacitive behavior (Figure 6d). Figure 6e displays the calculations of the specific capacitances for rGO according to the galvanostatic discharge curves. The specific capacitance for rGO can achieve a specific capacitance of 302 F g^{-1} at a current density of 1 A g^{-1}, and when the current density increases to 15 A g^{-1}, the specific capacitance can also achieve 121.5 F g^{-1}, indicating a good performance of rGO at high discharge rate. The cycling performance of rGO at a current density of 10 A g^{-1} is also shown in Figure 6f. The capacitance retention can remain as high as 95.4% of the maximum value after 5000 cycles, indicating the excellent cycling stability of the 3D porous graphene. The charge/discharge curves of the last 10 cycles of the rGO electrode are shown in the inset of Figure 6f, which exhibits a symmetrical linear characteristic, demonstrating a good EDLC performance.

3.3. Electrochemical Properties of the Asymmetric Supercapacitor. To further evaluate the honeycomb-like NiO electrode for practical applications, an asymmetric supercapacitor device has been designed and fabricated. In order to obtain a high performance of the NiO//rGO asymmetric supercapacitor device, the charge of the positive and negative electrodes should be optimized based on their testing results (for details, see the Supporting Information). Accordingly, the optimal mass ratio of rGO to NiO was adjusted to be about 1.8 for the NiO//rGO asymmetric supercapacitor based on the test results in the three-electrode system (the load weights of NiO and rGO are 2.65 and 4.8 mg cm^{-2}, respectively). The stored charge versus current density (Q−I) curves of the positive and negative electrodes and the full cell are shown in Figure S9. The shape of the Q−I curve of the full cell shows good similarity with the curves of the positive and negative electrodes, indicating that 1.8 is an appropriate mass ratio of rGO to NiO.

Figure 7a describes the CV curves of the NiO//rGO asymmetric supercapacitor device at different voltage windows in a 6 M KOH aqueous solution at a scan rate of 10 mV s^{-1}. The operation voltage window of the asymmetric supercapacitor device can be extended to 1.5 V. For an energy density is proportional to the square of the potential, the choice of a large potential window has the advantage of improving the overall electrochemical performance of the asymmetric supercapacitor over the symmetric supercapacitor. Figure 7b presents CV curves for the NiO//rGO asymmetric supercapacitor device at various scan rates between 0 and 1.5 V. The broad redox peaks were observed, indicating the faradaic pseudocapacitive nature of the NiO//rGO asymmetric supercapacitor arising from the NiO electrode. GCD tests were also performed to evaluate the electrochemical performance of the NiO//rGO asymmetric supercapacitor device at different current densities, as shown in Figure 7c. Figure 7d displays calculations of the specific capacitances of the asymmetric supercapacitor based on the total mass of the active materials of the two electrodes (with a total mass loading of the active material of about 8.4 mg). The specific capacitance for the asymmetric supercapacitor can achieve a specific capacitance of 74.4 F g^{-1} at a current density of 0.2 A g^{-1} (about 1.49 mA cm^{-2}), and when the current density increases to 10 A g^{-1} (about 74.5 mA cm^{-2}), about 58% of the specific capacitance is retained. The specific capacitance of the NiO//rGO asymmetric supercapacitor is higher than the values of NiO-based supercapacitors reported previously, such as 3D nanopetal-like NiO//AC (36.5 F g^{-1} and 0.5 A g^{-1}),[46] nanoflake NiO//rGO (50 F g^{-1} and 1 mA cm^{-2}),[47] and porous NiO//carbon (37 F g^{-1} and 1 mV s^{-1}).[20] The long-term specific capacitance retention of the asymmetric supercapacitor at a current density of 3 A g^{-1} after 2000 cycles was recorded, as shown in Figure 7d. The specific capacitance of the NiO//rGO asymmetric supercapacitor device can still be retained at about 88% after 2000 cycles, thus demonstrating the good cycling property of the as-prepared asymmetric supercapacitor device. Moreover, the NiO//rGO asymmetric supercapacitors can successfully light up a low-voltage LED, as shown in Figure S10 and the inset of Figure 7e.

Moreover, the performances of asymmetric supercapacitors with different mass ratios of rGO to NiO are measured for comparison. The CV curves of asymmetric supercapacitors at various scan rates with mass ratios of rGO to NiO of 1.5 and 2.2 are shown in Figure S11a,b. When the mass ratio is 1.5, there is a visible increment in the positive current (positive polarization) at a high voltage, which may be due to imbalanced charges between the negative and positive electrodes, leading to H_2 evolution at the rGO electrode. As the mass ratio increases to 1.8, no obvious positive polarization is found at the high voltage (Figure 7b). Especially, a significant redox peak appears at the mass ratio of 2.2, indicating a battery-like behavior dominating in this hybrid device. Figure S11c displays the rate capability of asymmetric supercapacitors. As the mass ratio increases, the rate capability improves. However, the hybrid device shows the best capacitance performance at the mass ratio of 1.8. The cycling performances of the asymmetric supercapacitors at different rGO/NiO mass ratios are shown in Figure S11d. The supercapacitor at the mass ratio of 1.8 displays the best cycling stability, indicating the appropriate

DOI: 10.1021/acsami.5b04094
ACS Appl. Mater. Interfaces 2015, 7, 19930−19940

mass ratio of positive to negative electrodes and excellent reversibility during the charge and discharge processes.

The energy and power densities are the two key parameters in characterizing the performances of supercapacitors. Figure 7f displays Ragone plots of the NiO//rGO asymmetric supercapacitor device based on the GCD tests. The energy density of the device decreases from 23.25 to 13.51 Wh kg^{-1} as the power density increases from 151 to 9324 W kg^{-1}, which are much higher than those of NiO-based asymmetric supercapacitors, such as NiO//carbon,[20] NiO//AC,[46] and rGO//rGO symmetric supercapacitors.[48] Although the energy and power densities of the NiO//rGO asymmetric supercapacitors are lower than some other materials for asymmetric supercapacitors, such as $NiCo_2O_4$@MnO_2//AC,[49] $Co(OH)_2$//VN,[50] and V_2O_5//C,[51] the NiO materials have the great advantages of low cost, environmental friendliness, and ease of preparation. Thus, the NiO//rGO asymmetric supercapacitor device is a potential alternative for commercial supercapacitors.

4. CONCLUSION

In conclusion, the hierarchical self-assembled NiO is prepared via a two-step process including a simple hydrothermal method and a subsequent calcination process in air. The morphologies of NiO can be controlled by the pH in the hydrothermal route, and the hierarchical honeycomb-like NiO microsphere with a high specific surface area (257 m^2 g^{-1}) and a large pore volume (1.64 cm g^{-1}) displays the best supercapacitor property. Their specific capacitance for the honeycomb-like NiO electrode can reach as high as 1250 F g^{-1} at a current density of 1 A g^{-1} and still remains 835 F g^{-1} after 3500 cycles at 5 A g^{-1}. Additionally, the NiO//rGO asymmetric supercapacitor can deliver a prominent energy density of 23.25 Wh kg^{-1} at a power density of 151 W kg^{-1}, and it can also operate at a high power density of 9.3 kW kg^{-1} with an energy density of 13.5 Wh kg^{-1}. These findings indicate great promise for further electrochemical applications in supercapacitors.

■ ASSOCIATED CONTENT

Supporting Information

The Supporting Information is available free of charge on the ACS Publications website at DOI: 10.1021/acsami.5b04094.

Additional experimental data as described in the text (PDF)

■ AUTHOR INFORMATION

Corresponding Authors

*Tel: +86 351 6018683. Fax: +86 351 6018683. E-mail: guochunli@tyut.edu.cn.

*Tel: +86 351 6018683. Fax: +86 351 6018683. E-mail: weiyinghui@tyut.edu.cn.

Author Contributions

The manuscript was written through contributions of all authors. All authors have given approval to the final version of the manuscript.

Notes

The authors declare no competing financial interest.

■ ACKNOWLEDGMENTS

The authors acknowledge the National Science Foundation of China (Grants 51374151, 21201129, and 21471091), the Major Project for Science & Technology of Shanxi Province (Grant 20111101053), the Key Project for Science & Technology of coal base research in Shanxi Province and the Natural Science Foundation of Shanxi Province (Grants 2011011020-2 and 2013011012-3), the 973 Project of China (Grant 2011CB935901), and the Fundamental Research Funds of Shandong University (Grant 2015JC007) for providing funding support to the current work.

■ REFERENCES

(1) Winter, M.; Brodd, R. J. What Are Batteries, Fuel Cells, and Supercapacitors? *Chem. Rev.* **2004**, *104*, 4245−4269.

(2) Hall, P. J.; Mirzaeian, M.; Fletcher, S. I.; Sillars, F. B.; Rennie, A. J. R.; Shitta-Bey, G. O.; Wilson, G.; Cruden, A.; Carter, R. Energy Storage in Electrochemical Capacitors: Designing Functional Materials to Improve Performance. *Energy Environ. Sci.* **2010**, *3*, 1238−1251.

(3) Simon, P.; Gogotsi, Y. Materials for Electrochemical Capacitors. *Nat. Mater.* **2008**, *7*, 845−854.

(4) Wang, G.; Zhang, L.; Zhang, J. A Review of Electrode Materials for Electrochemical Supercapacitors. *Chem. Soc. Rev.* **2012**, *41*, 797−828.

(5) Zhang, L. L.; Zhao, X. S. Carbon-based Materials as Supercapacitor Electrodes. *Chem. Soc. Rev.* **2009**, *38*, 2520−2531.

(6) Lv, Y.; Gan, L.; Liu, M.; Xiong, W.; Xu, Z.; Zhu, D.; Wright, D. S. A Self-template Synthesis of Hierarchical Porous Carbon Foams Based on Banana Peel for Supercapacitor Electrodes. *J. Power Sources* **2012**, *209*, 152−157.

(7) Sharma, P.; Bhatti, T. S. A Review on Electrochemical Double-layer Capacitors. *Energy Convers. Manage.* **2010**, *51*, 2901−2912.

(8) Gurav, K. V.; Patil, U. M.; Shin, S. W.; Agawane, G. L.; Suryawanshi, M. P.; Pawar, S. M.; Patil, P. S.; Lokhande, C. D.; Kim, J. H. Room Temperature Chemical Synthesis of $Cu(OH)_2$ Thin Films for Supercapacitor Application. *J. Alloys Compd.* **2013**, *573*, 27−31.

(9) Hu, C.-C.; Chen, J.-C.; Chang, K.-H. Cathodic Deposition of $Ni(OH)_2$ and $Co(OH)_2$ for Asymmetric Supercapacitors: Importance of the Electrochemical Reversibility of Redox Couples. *J. Power Sources* **2013**, *221*, 128−133.

(10) Yang, L.; Cheng, S.; Ding, Y.; Zhu, X.; Wang, Z. L.; Liu, M. Hierarchical Network Architectures of Carbon Fiber Paper Supported Cobalt Oxide Nanonet for High-capacity Pseudocapacitors. *Nano Lett.* **2012**, *12*, 321−325.

(11) Yuan, C.; Zhang, X.; Su, L.; Gao, B.; Shen, L. Facile Synthesis and Self-assembly of Hierarchical Porous NiO Nano/micro Spherical Superstructures for High Performance Supercapacitors. *J. Mater. Chem.* **2009**, *19*, 5772−5777.

(12) Zhang, K.; Zhang, L. L.; Zhao, X. S.; Wu, J. Graphene/Polyaniline Nanofiber Composites as Supercapacitor Electrodes. *Chem. Mater.* **2010**, *22*, 1392−1401.

(13) He, J.; Zhao, Y.; Xiong, D.-B.; Ran, W.; Xu, J.; Ren, Y.; Zhang, L.; Tang, Y.; Gao, F. Biotemplate Assisted Synthesis of 3D Hierarchical Porous NiO for Supercapatior Application with Excellent Rate Performance. *Mater. Lett.* **2014**, *128*, 117−120.

(14) Ding, S.; Zhu, T.; Chen, J. S.; Wang, Z.; Yuan, C.; Lou, X. W. Controlled Synthesis of Hierarchical NiO Nanosheet Hollow Spheres with Enhanced Supercapacitive Performance. *J. Mater. Chem.* **2011**, *21*, 6602−6606.

(15) Li, J.; Luo, F.; Zhao, Q.; Li, Z.; Yuan, H.; Xiao, D. Coprecipitation Fabrication and Electrochemical Performances of Coral-like Mesoporous NiO Nanobars. *J. Mater. Chem. A* **2014**, *2*, 4690−4697.

(16) Huang, M.; Li, F.; Ji, J. Y.; Zhang, Y. X.; Zhao, X. L.; Gao, X. Facile Synthesis of Single-crystalline NiO Nanosheet Arrays on Ni Foam for High-performance Supercapacitors. *CrystEngComm* **2014**, *16*, 2878−2884.

(17) Yan, X.; Tong, X.; Wang, J.; Gong, C.; Zhang, M.; Liang, L. Synthesis of Mesoporous NiO Nanoflake Array and Its Enhanced Eelectrochemical Performance for Supercapacitor Application. *J. Alloys Compd.* **2014**, *593*, 184−189.

DOI: 10.1021/acsami.5b04094
ACS Appl. Mater. Interfaces 2015, 7, 19930−19940

(18) Du, D.; Hu, Z.; Liu, Y.; Deng, Y.; Liu, J. Preparation and Characterization of Flower-like Microspheres of Nano-NiO as Electrode Material for Supercapacitor. *J. Alloys Compd.* **2014**, *589*, 82−87.
(19) Wang, Y.-g.; Xia, Y.-y. Electrochemical Capacitance Characterization of NiO with Ordered Mesoporous Structure Synthesized by Template SBA-15. *Electrochim. Acta* **2006**, *51*, 3223−3227.
(20) Wang, D.-W.; Li, F.; Cheng, H.-M. Hierarchical Porous Nickel Oxide and Carbon as Electrode Materials for Asymmetric Supercapacitor. *J. Power Sources* **2008**, *185*, 1563−1568.
(21) Li, Y.; Xie, X.; Liu, J.; Cai, M.; Rogers, J.; Shen, W. Synthesis of α-Ni(OH)2 with Hydrotalcite-like Structure: Precursor for the Formation of NiO and Ni Nanomaterials with Fibrous Shapes. *Chem. Eng. J.* **2008**, *136*, 398−408.
(22) Varghese, B.; Reddy, M. V.; Yanwu, Z.; Lit, C. S.; Hoong, T. C.; Rao, G. V. S.; Chowdari, B. V. R.; Wee, A. T. S.; Lim, C. T.; Sow, C. H. Fabrication of NiO Nanowall Electrodes for High Performance Lithium Ion Battery. *Chem. Mater.* **2008**, *20*, 3360−3367.
(23) Liang, K.; Tang, X.; Hu, W. High-Performance Three-Dimensional Nanoporous NiO Film as a Supercapacitor Electrode. *J. Mater. Chem.* **2012**, *22*, 11062−11067.
(24) Manders, J. R.; Tsang, S. W.; Hartel, M. J.; Lai, T. H.; Chen, S.; Amb, C. M.; Reynolds, J. R.; So, F. Solution-Processed Nickel Oxide Hole Transport Layers in High Efficiency Polymer Photovoltaic Cells. *Adv. Funct. Mater.* **2013**, *23*, 2993−3001.
(25) Lei, Y.; Li, J.; Wang, Y.; Gu, L.; Chang, Y.; Yuan, H.; Xiao, D. Rapid Microwave-assisted Green Synthesis of 3D Hierarchical Flower-shaped $NiCo_2O_4$ Microsphere for High-performance Supercapacitor. *ACS Appl. Mater. Interfaces* **2014**, *6*, 1773−1780.
(26) Li, L.; Cheah, Y.; Ko, Y.; Teh, P.; Wee, G.; Wong, C.; Peng, S.; Srinivasan, M. The Facile Synthesis of Hierarchical Porous Flower-like $NiCo_2O_4$ with Superior Lithium Storage Properties. *J. Mater. Chem. A* **2013**, *1*, 10935−10941.
(27) Cao, C.-Y.; Guo, W.; Cui, Z.-M.; Song, W.-G.; Cai, W. Microwave-assisted Gas/liquid Interfacial Synthesis of Flowerlike NiO Hollow Nanosphere Precursors and Their Application as Supercapacitor Electrodes. *J. Mater. Chem.* **2011**, *21*, 3204−3209.
(28) Sangwichien, C.; Aranovich, G. L.; Donohue, M. D. Density Functional Theory Predictions of Adsorption Isotherms with Hysteresis Loops. *Colloids Surf., A* **2002**, *206*, 313−320.
(29) He, X.; Yang, M.; Ni, P.; Li, Y.; Liu, Z.-H. Rapid Synthesis of Hollow Structured MnO_2 Microspheres and Their Capacitance. *Colloids Surf., A* **2010**, *363*, 64−70.
(30) Gnana Sundara Raj, B.; Asiri, A. M.; Qusti, A. H.; Wu, J. J.; Anandan, S. Sonochemically Synthesized MnO_2 Nanoparticles as Electrode Material for Supercapacitors. *Ultrason. Sonochem.* **2014**, *21*, 1933−1938.
(31) Yu, C.; Zhang, L.; Shi, J.; Zhao, J.; Gao, J.; Yan, D. A Simple Template-Free Strategy to Synthesize Nanoporous Manganese and Nickel Oxides with Narrow Pore Size Distribution, and Their Electrochemical Properties. *Adv. Funct. Mater.* **2008**, *18*, 1544−1554.
(32) Xia, K.; Gao, Q.; Jiang, J.; Hu, J. Hierarchical Porous Carbons with Controlled Micropores and Mesopores for Supercapacitor Electrode Materials. *Carbon* **2008**, *46*, 1718−1726.
(33) Korenblit, Y.; Rose, M.; Kockrick, E.; Borchardt, L.; Kvit, A.; Kaskel, S.; Yushin, G. High-Rate Electrochemical Capacitors Based on Ordered Mesoporous Silicon Carbide-Derived Carbon. *ACS Nano* **2010**, *4*, 1337−1344.
(34) Xu, X.; Liang, J.; Zhou, H.; Ding, S.; Yu, D. The Preparation of Hierarchical Tubular Structures Comprised of NiO Nanosheets with Enhanced Supercapacitive Performance. *RSC Adv.* **2014**, *4*, 3181−3187.
(35) Kim, S. I.; Lee, J. S.; Ahn, H. J.; Song, H. K.; Jang, J. H. Facile Route to an Efficient NiO Supercapacitor with a Three-dimensional Nanonetwork Morphology. *ACS Appl. Mater. Interfaces* **2013**, *5*, 1596−1603.
(36) Singh, A. K.; Sarkar, D.; Khan, G. G.; Mandal, K. Hydrogenated NiO Nanoblock Architecture for High Performance Pseudocapacitor. *ACS Appl. Mater. Interfaces* **2014**, *6*, 4684−4692.
(37) Purushothaman, K. K.; Manohara Babu, I.; Sethuraman, B.; Muralidharan, G. Nanosheet-assembled NiO Microstructures for High-performance Supercapacitors. *ACS Appl. Mater. Interfaces* **2013**, *5*, 10767−10773.
(38) Cao, F.; Pan, G. X.; Xia, X. H.; Tang, P. S.; Chen, H. F. Synthesis of Hierarchical Porous NiO Nanotube Arrays for Supercapacitor Application. *J. Power Sources* **2014**, *264*, 161−167.
(39) Yao, M.; Hu, Z.; Xu, Z.; Liu, Y.; Liu, P.; Zhang, Q. High-performance Electrode Materials of Hierarchical Mesoporous Nickel Oxide Ultrathin Nanosheets Derived from Self-assembled Scroll-like α-nickel Hydroxide. *J. Power Sources* **2015**, *273*, 914−922.
(40) Gund, G. S.; Dubal, D. P.; Shinde, S. S.; Lokhande, C. D. Architectured Morphologies of Chemically Prepared NiO/MWCNTs Nanohybrid Thin Films for High Performance Supercapacitors. *ACS Appl. Mater. Interfaces* **2014**, *6*, 3176−3188.
(41) Wang, D. W.; Li, F.; Liu, M.; Lu, G. Q.; Cheng, H. M. 3D Aperiodic Hierarchical Porous Graphitic Carbon Material for High-Rate Electrochemical Capacitive Energy Storage. *Angew. Chem., Int. Ed.* **2008**, *47*, 373−376.
(42) Xia, X.; Tu, J.; Zhang, Y.; Wang, X.; Gu, C.; Zhao, X.-b.; Fan, H. High-Quality Metal Oxide Core/Shell Nanowire Arrays on Conductive Substrates for Electrochemical Energy Storage. *ACS Nano* **2012**, *6*, 5531−5538.
(43) Mai, L.; Li, H.; Zhao, Y.; Xu, L.; Xu, X.; Luo, Y.; Zhang, Z.; Ke, W.; Niu, C.; Zhang, Q. Fast Ionic Diffusion-Enabled Nanoflake Electrode by Spontaneous Electrochemical Pre-Intercalation for High-Performance Supercapacitor. *Sci. Rep.* **2013**, *3*, 1718.
(44) Liu, W.-w.; Yan, X.-b.; Lang, J.-w.; Pu, J.-b.; Xue, Q.-j. Supercapacitors Based on Graphene Nanosheets Using Different Non-Aqueous Electrolytes. *New J. Chem.* **2013**, *37*, 2186−2195.
(45) Moon, I. K.; Lee, J.; Ruoff, R. S.; Lee, H. Reduced Graphene Oxide by Chemical Graphitization. *Nat. Commun.* **2010**, *1*, 73.
(46) Cheng, G.; Bai, Q.; Si, C.; Yang, W.; Dong, C.; Wang, H.; Gao, Y.; Zhang, Z. Nickel Oxide Nanopetal-Decorated 3D Nickel Network with Enhanced Pseudocapacitive Properties. *RSC Adv.* **2015**, *5*, 15042−15051.
(47) Luan, F.; Wang, G.; Ling, Y.; Lu, X.; Wang, H.; Tong, Y.; Liu, X. X.; Li, Y. High Energy Density Asymmetric Supercapacitors with a Nickel Oxide Nanoflake Cathode and a 3D Reduced Graphene Oxide Anode. *Nanoscale* **2013**, *5*, 7984−7990.
(48) Xu, Y.; Lin, Z.; Huang, X.; Liu, Y.; Huang, Y.; Duan, X. Flexible Solid-State Supercapacitors Based on Three-Dimensional Graphene Hydrogel Films. *ACS Nano* **2013**, *7*, 4042−4049.
(49) Xu, K.; Li, W.; Liu, Q.; Li, B.; Liu, X.; An, L.; Chen, Z.; Zou, R.; Hu, J. Hierarchical Mesoporous $NiCo_2O_4$@MnO_2 Core−shell Nanowire Arrays on Nickel Foam for Aqueous Asymmetric Supercapacitors. *J. Mater. Chem. A* **2014**, *2*, 4795−4802.
(50) Wang, R.; Yan, X.; Lang, J.; Zheng, Z.; Zhang, P. A Hybrid Supercapacitor Based on Flower-like $Co(OH)_2$ and Urchin-like VN Electrode Materials. *J. Mater. Chem. A* **2014**, *2*, 12724−12732.
(51) Lin, Z.; Yan, X.; Lang, J.; Wang, R.; Kong, L.-B. Adjusting Electrode Initial Potential to Obtain High-Performance Asymmetric Supercapacitor Based on Porous Vanadium Pentoxide Nanotubes and Activated Carbon Nanorods. *J. Power Sources* **2015**, *279*, 358−364.

DOI: 10.1021/acsami.5b04094
ACS Appl. Mater. Interfaces 2015, 7, 19930−19940